Cislunar Surveillance Optimization and Key Region Identification

Surabhi Bhadauria, Arly Black, and Carolin Frueh
Purdue University

ABSTRACT

Cislunar space's growing importance necessitates robust space domain awareness for its safe and sustainable utilization. Current ground-based surveillance is insufficient to cover the entire cislunar region of interest, leaving large blind spots. Space-based optical sensors can address this, but due to the vastness of the cislunar space and particular regions of higher interest, sensor placement is complex. This paper proposes an optimized sensor distribution strategy for Cislunar Space Domain Awareness (CSDA), to maintain custody of significant objects in the presence of possible unknown maneuvers at unknown times. As examples, this work focuses on key regions deviating from L_2 Lyapunov and Near Rectilinear Halo Orbits (NRHO), with maneuver sizes of 0.05 km/s Δv to 0.5 km/s Δv. Using dynamical deviation flow in the Circular Restricted Three-Body Problem (CR3BP), critical surveillance regions are identified. The optimal sensor locations are determined via Particle Swarm Optimization (PSO), utilizing the average visibility to enhance CSDA capabilities.

1. INTRODUCTION

Cislunar space has become a target for many current and future missions [1], accelerating the need for comprehensive space domain awareness in the region. Presently, modern ground-based surveillance capabilities are severely lacking, revealing large regions of blindness to any activity, or regions where surveillance can be established under only the most ideal conditions [11, 14]. Space-based optical sensors can aid in remedying this situation. However, previous studies have shown that the parameter space for the placement of a given number of sensors is tremendous [2, 3], and ad hoc point solutions – while intuitive – might not provide the most cost and performance efficient satellite network locations or may miss out on key locations. One of the challenges of keeping track of objects in cislunar space is that, even for initially detected and known objects, small orbital maneuvers and departures can give access to entirely different regions of space, due to the chaotic nature of system dynamics in the cislunar domain [5], allowing for fast departure from the parent orbit. Small maneuvers at unknown times can lead to immediate loss of supervision of even initially known and detected objects.

To address these challenges, dynamical deviation flow is used to identify key surveillance regions in cislunar space. This is achieved by finding orbital departure tubes in the Circular Restricted Three Body Problem (CR3BP), for two representative L_2 orbits and two Δv maneuver magnitudes of 0.05 km/s and 0.5 km/s. Despite the chaotic nature of the cislunar region for small bodies, finding departure tubes enables location of regions the object must traverse post-maneuver, even if the exact maneuver time and size remain unknown. Flow prediction is valuable for passively maintaining custody of objects in the region, including assessing mission intent and enabling tracking of satellites with communication issues. In a second step, the target objects spanned by the maneuvering orbits are mapped to a predefined set of points in the cislunar region. All the points are equidistant within the sphere of influence of the Earth [23] and are taken as potential sensor locations. The average visibility is evaluated for the mapped locations from all the sensor locations using the parameterization offered by the geometry of in-plane the Bi-Circular Four Body Problem (BCR4BP). Finally, the optimal optical observers are produced by the Particle Swarm Optimization (PSO) by leveraging the average visibility from each sensors.

This paper leverages dynamic departure tubes to identify volumetric regions in cislunar space for which surveillance is crucial in order to capture the extent of varying deviation magnitudes, and locates optimal observer locations. A hybrid of the CR3BP and the BCR4BP is employed, which allows a parameterization of the problem and a global optimization in terms of flow and visibility constraints. This study offers optimized and efficient sensor distribution to regions spanned by small orbit maneuvers applied to a planar L_2 Lyapunov orbit and a Near Rectilinear Halo Orbit (NRHO). A focus of this paper are electro-optical sensors because of their relatively low power constraints, ease of deployment, and overall cost.

2. DYNAMICAL MODELS

The cislunar regime is dominated by a number of gravitational bodies, predominantly the Earth, the Moon, and the Sun. In this investigation, we make use of the traditional three and four body problem approximations of the CR3BP and the BCR4BP. The accuracy of these models relative to high-fidelity ephemeris models have been studied in [11, 12], showing the applicability for this study. Here, the CR3BP is used to model the motion of objects in the Earth-Moon system and the BCR4BP is engaged to obtain illumination information.

2.1 Circular Restricted Three Body Problem

The CR3BP considers the motion of a satellite of negligible mass subjected to the gravitational forces of two large primary bodies rotating in circular orbits about their common center of mass, or Barycenter, at a constant rate [27]. The CR3BP is conveniently expressed in a non-dimensional, synodic reference frame that rotates with the primaries, where the x-axis is directed along the vector pointing from the larger body with mass m_1 to the smaller body of mass m_2, the y-axis is orthogonal to the x-axis and lies in the rotating plane, and the z-axis lies normal to the rotating plane. The system is non-dimensionalized such that both the distance between the two primaries and the mean motion of the primaries are equal to one. The second-order, nonlinear CR3BP equations of motion are defined as [27, 16]

$$\ddot{x} = 2\dot{y} + \frac{\partial U^*}{\partial x} \qquad \ddot{y} = -2\dot{x} + \frac{\partial U^*}{\partial y} \qquad \ddot{z} = \frac{\partial U^*}{\partial z}, \tag{1}$$

where $\bar{\mathbf{x}} = [x,\, y,\, z,\, \dot{x},\, \dot{y},\, \dot{z}]^T$ represents the non-dimensional (nd) state vector of the particle, or third body, in rotating coordinates, and U^* represents the gravitational pseudo-potential of the system, calculated by

$$U^* = \frac{1}{2}(x^2 + y^2) + \frac{1-\mu}{r_{13}} + \frac{\mu}{r_{23}} \tag{2}$$

The constant $\mu = m_2/(m_1 + m_2)$ is the non-dimensional mass parameter, while $r_{13} = \sqrt{(x+\mu)^2 + y^2 + z^2}$ and $r_{23} = \sqrt{(x-1+\mu)^2 + y^2 + z^2}$ are the distances between the respective primaries and the third body. The equations of motion of the CR3BP yield a single integral of the motion, an energy-like quantity known as the *Jacobi constant JC*, defined as

$$JC = 2U^* - (\dot{x}^2 + \dot{y}^2 + \dot{z}^2) \tag{3}$$

where the first and second terms represent potential energy and kinetic energy, respectively. JC is inversely proportional to energy, such that a higher JC corresponds to a lower energy, and vice versa. Five equilibrium locations, named Lagrange or libration points L_1 to L_5, exist in the CR3BP rotating plane; the collinear libration points L_1, L_2 and L_3 lie along the x-axis and equilateral points L_4 and L_5 form vertices of an equilateral triangle with the two primaries. In the vicinity of the respective Lagrange points, there exist families of infinite periodic or quasi-periodic libration point orbits (LPO). Unstable LPOs possess stable and unstable invariant manifolds which facilitate asymptotic ballistic arrival and departure pathways to and from the orbit.

Zero Velocity Curves (ZVCs) are continuous surface boundaries that dictate forbidden regions for an orbiting object within the CR3BP. As object energy increases (corresponding to a decreasing JC), ZVC volumes are reduced and objects may move more freely through cislunar space. Each libration point has an associated JC and accompanying ZVC, and objects require sufficient energy in order to transit through those regions.

One valuable instrument in the CR3BP toolkit is the Poincaré map – a classical method of reducing the dimensionality of a state space to facilitate visualization of emergent patterns or structures in the dynamics. This is achieved through the strategic application of hyperplanes Σ defined at a physical location transverse to the flow of the system, whereby crossings of Σ are recorded [19]. Poincaré maps exhibit properties unique to periodic and quasi-periodic orbits, and can simplify characteristics of system dynamics that may not be obvious or apparent in configuration space.

2.2 Bicircular Restricted Four Body Problem

To accurately assess the illumination conditions essential for satellite surveillance, the Sun's position must be factored into the visibility model. This paper employs the geometry of the in-plane BCR4BP to parameterize the motion of primary bodies—Earth, Moon, and Sun—that influence the visibility of targets in cislunar space. BCR4BP analyzes the dynamics of an artificial satellite under the gravitational effects of the Earth-Moon-Sun system [6, 27, 15, 18]. Figure 1 depicts the planar BCR4BP model, where an infinitesimal mass (m_3) is affected by the Earth (m_1), Moon

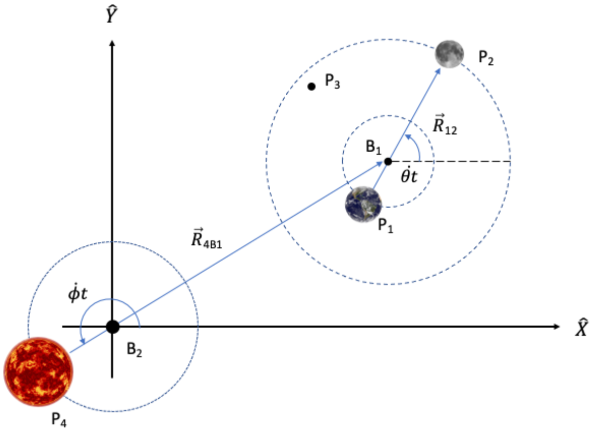

Fig. 1: Planar BCR4BP model with the Sun, the Earth, and the Moon as the primaries.

(m_2), and Sun (m_4). The locations of these bodies are represented as P_1, P_2, P_3 and P_4, respectively, with $m_4 > m_1 > m_2 > m_3$. The primary axes, $\hat{X}$, $\hat{Y}$, and $\hat{Z}$, are defined in an inertial reference frame originating at the Earth-Moon-Sun Barycenter (B_2). The Earth and Moon move in circular orbits around their common Barycenter (B_2), while the Sun and Earth-Moon Barycenter move in circular orbits around the Sun-Earth-Moon Barycenter (B_2), all within the same orbital plane. The initial angles of the Moon and Sun relative to the inertial $\hat{X}$ axis are denoted by θ_0 and ϕ_0, which change with angular velocities $\dot{\theta}$ and $\dot{\phi}$, respectively.

2.2.1 Parameterization of Cislunar Space Using BCR4BP Geometry

The repetitive geometry resulting from the motion of the primary bodies in the BCR4BP model can be leveraged to develop a straightforward visibility parameterization [4]. The position vectors $\vec{R}_{B_1 1}$ and $\vec{R}_{B_1 2}$, representing the Earth and Moon relative to the Earth-Moon Barycenter, are given by

$$\vec{R}_{B_1 1} = |\vec{R}_{B_1 1}|(-\cos(\dot{\theta}t+\theta_0)\hat{X} - \sin(\dot{\theta}t+\theta_0)\hat{Y}), \tag{4}$$

$$\vec{R}_{B_1 2} = |\vec{R}_{B_1 2}|(\cos(\dot{\theta}t+\theta_0)\hat{X} + \sin(\dot{\theta}t+\theta_0)\hat{Y}). \tag{5}$$

Given the Sun's angular velocity $\dot{\phi}$ relative to the inertial $\hat{X}$ axis, the positions of the Earth-Moon Barycenter (B_1), $\vec{R}_{B_2 B_1}$, and the Sun, $\vec{R}_{B_2 4}$, relative to the system Barycenter B_2 are

$$\vec{R}_{B_2 B_1} = |\vec{R}_{B_2 B_1}|(-\cos(\dot{\phi}t+\phi_0)\hat{X} - \sin(\dot{\phi}t+\phi_0)\hat{Y}), \tag{6}$$

$$\vec{R}_{B_2 4} = |\vec{R}_{B_2 4}|(\cos(\dot{\phi}t+\phi_0)\hat{X} + \sin(\dot{\phi}t+\phi_0)\hat{Y}). \tag{7}$$

By combining $\vec{R}_{B_2 4}$ and $\vec{R}_{B_2 B_1}$, the Sun's position relative to the Earth-Moon Barycenter (B_1) can be determined. These formulations of the primary bodies' positions using BCR4BP parameters are essential for assessing the visibility conditions of space objects.

3. VISIBILITY CONSTRAINTS

The optical constraints considered in this paper include exclusion angle zones from the primary bodies and the telescope's limiting magnitude. These constraints are derived from Bhadauria et al. [4] and are repeated here for the completeness of the paper. Figure 2 depicts the optical angles that influence visibility constraints. The Earth is located at P_1, the Moon at P_2, the Sun at P_4, the object at P_3, and the observer at P_5. The exclusion angles from the Earth (α), Moon (β), and Sun (γ) are observed from the observer's position, while the phase angle (δ) between the Sun and the observer is viewed from the object's location. Further details on these visibility constraints are available in [4].

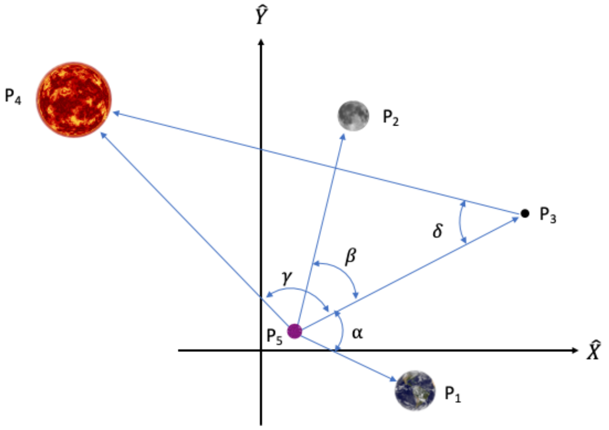

Fig. 2: Illustration of the phase angle (δ) between the Sun and the observer, object's angle with respect to the Earth (α), object's angle with respect to the Moon (β), and object's angle with respect to the Sun (γ).

3.1 Magnitude Constraint

The magnitude [10, 4] of a representative space object is computed to model its brightness from an optical sensor and is expressed as

$$\text{mag}_{\text{object}} = \text{mag}_{\text{sun}} - 2.5\log_{10}\left(\frac{I_{\text{object}}}{I_{\text{sun}}}\right) \tag{8}$$

where mag_{sun} is the apparent reference magnitude of the Sun, I_{object} is the irradiance reflected off the spacecraft and I_{Sun} is the Sun's reference irradiance. The irradiance of an objects depends on its albedo, area, shape, and attitude. For this paper, a cannonball model is assumed, with a radius of one meter and Lambertian reflectivity of 0.5. Although this model neglects glints, it provides a reasonable baseline for visibility conditions. While a box-wing satellite model would account for glints, these only occur at small phase angles for operational satellites in Sun-oriented configurations and may not always be illuminated. The object's illumination is influenced by the phase angle (δ) between the Sun and the observer, measured from the object.

A limiting magnitude constraint, denoted as $\text{mag}_{\text{limit}}$, is applied such that objects brighter than $\text{mag}_{\text{limit}}$ are visible, with a value of 18 chosen for this paper. The limiting magnitude depends on factors such as background noise, exposure time, atmospheric turbulence, image processing methods, and the optical system itself [13, 10, 21, 22].

$$V_{(\text{mag})} = \begin{cases} 1 \text{ if } \text{mag}_{\text{object}} < \text{mag}_{\text{limit}} \\ 0, \text{otherwise} \end{cases} \tag{9}$$

3.2 Exclusion Zones

The primary bodies in the cislunar region—the Sun, Earth, and Moon—influence observations based on their relative positions to the object and the observer. Therefore, visibility constraints are established through exclusion zones related to these celestial bodies [4].

The Earth's exclusion angle (α) in Fig. 2 is defined as the angle between the object's position and Earth's position as viewed by the observer ($\alpha = \angle(\vec{R}_{53}, \vec{R}_{51})$). The object is visible within the Earth's exclusion zone (EEZ) if α exceeds 10°.

$$V_{(\text{EEZ})} = \begin{cases} 1 \text{ if } \alpha > 10^\circ \\ 0, \text{otherwise} \end{cases} \tag{10}$$

The Moon's exclusion angle (β) is defined similarly as the angle between the object's position and the Moon's position when viewed by the observer ($\beta = \angle(\vec{R}_{53}, \vec{R}_{52})$). The object is visible within the Moon's exclusion zone (MEZ) if β

is greater than 10°.

$$V_{(\text{MEZ})} = \begin{cases} 1 \text{ if } \beta > 10^\circ \\ 0, \text{otherwise} \end{cases} \tag{11}$$

The Sun's exclusion angle (γ) is defined as the angle between the object's position and the Sun's position as seen by the observer ($\gamma = \angle(\vec{R}_{53}, \vec{R}_{54})$). The object is considered visible within the Sun's exclusion zone (SEZ) if γ is greater than 30°.

$$V_{(\text{SEZ})} = \begin{cases} 1 \text{ if } \gamma > 30^\circ \\ 0, \text{otherwise} \end{cases} \tag{12}$$

3.3 Visibility Count Percentage

The visibility count percentage (VCP) quantifies the visibility of an object over time, defined as the percentage of time steps during which the object is visible out of the total observation time. VCP can be calculated for individual constraints (e.g., limiting magnitude, exclusion angles for the Sun, Moon, and Earth) or for all constraints combined. The formula for VCP considers the number of observers and the time steps when the object is visible. VCP_{single} refers to visibility from a single observer, while VCP_{all} is the average visibility across multiple observers in a discretized cislunar region. A score of 100 indicates full visibility from all observers. VCP_{all} is computationally efficient and used to generate visibility maps. With the application of VCP, Particle Swarm Optimization (PSO) helps identify optimal observer locations for adequate visibility in cislunar space. Mathematically, VCP is expressed as [4]

$$VCP = \frac{1}{n} \sum_{i}^{n} \frac{t_{\text{visible},i}}{t_{\text{all}}} \cdot 100, \tag{13}$$

where n represents the number of observers, $t_{\text{visible,i}}$ are the time steps at which the object is visible from the i^{th} observer and t_{all} are the total number of time steps.

4. PARTICLE SWARM OPTIMIZATION

Particle Swarm Optimization (PSO) is a computational technique used to optimize an objective function by iteratively refining the positions of candidate solutions, known as particles, within a search space. Inspired by the social behavior of bird flocks and insect swarms, PSO was introduced by Kennedy, Eberhart, and Shi [17, 24] in 1995. Each particle represents a potential solution to the optimization problem. During each iteration, the objective function value for each particle is evaluated and compared to its local best position and the global best position found by the swarm. The particle's position is then updated by adjusting its velocity, which guides it towards both the local and global best positions.

In this study, visibility maps based on the VCP provide information about the visibility of all defined objects from each observer location in the cislunar region. PSO is employed from Bhadauria et al. [4] to maximize the number of visible objects from a set of predefined observers by iteratively adjusting their positions. The objective function for this visibility optimization problem is defined as

$$f(r) = \{\cup(\text{objects visible by } i^{th} \text{ observer where i } = 1, 2, 3, \ldots, n)\} \tag{14}$$

where r represents each particle as

$$r = \{r_{x1}, r_{y1}, r_{z1}, r_{x2}, r_{y2}, r_{z2}, \ldots, r_{xi}, r_{yi}, r_{zi}\} \tag{15}$$

and $\{r_{x1}, r_{y1}, r_{z1}\}$ is the position of the first observer, $\{r_{x2}, r_{y2}, r_{z2}\}$ is the position of the second observer, and r_{xi}, r_{yi}, r_{zi} is the position of the i^{th} observer. Each particle has a dimensionality of $3 \times i$, and the spatial components of each particle are constrained within -400,000 to 400,000 km. Since the VCP maps are defined for discrete points, the objective function is calculated using the closest predefined observer location to the continuously updated observer position. The algorithm then determines the VCP_{single} for each observer and identifies the visible objects from all observers collectively. The precomputed VCP_{single} values from the visibility maps reduce computational cost significantly. The PSO algorithm ultimately yields an optimal set of observer positions that maximize visibility coverage.

5. INVESTIGATION OF KEY REGIONS AND SURVEILLANCE SCENARIOS

5.1 Orbital Regions and Surveillance Overview

The following investigation is concerned with characterizing and observing deviations from valuable cislunar orbits. Perturbations can arise from natural forces, controlled maneuvers, or unexpected fragmentation events, although in this work we assume maneuver scenarios, as these are more likely in practice. It is advantageous to assign a level of predictability to the motion of a spacecraft after it has performed a maneuver, in case, for example, communication is later lost or to judge mission intent of an adversarial spacecraft. Predictability is especially difficult in the dynamically complex cislunar regime.

L_2 orbits have arisen as popular mission destinations for their communications coverage of the far side of Moon and lunar poles [9], low-cost orbit accessibility offered by natural manifold structures, and the L_2 point's role as a gateway between the cislunar region and distant interplanetary targets [26]. The L_2 Lyapunov orbit family lies entirely in the CR3BP rotating plane, while the L_2 halo orbit family emerges as a bifurcation from the planar L_2 Lyapunov orbits in both positive z (northern) and negative z (southern) configurations. Near Rectilinear Halo Orbits (NRHO) are a subset of the halo orbit family that are nearly stable, defined by the bounds of bifurcations in halo orbit linear stability [28], and are thus desirable as staging areas for future lunar missions, including NASA's Lunar Gateway. In the following cislunar surveillance analysis, we analyze the common bifurcating planar L_2 Lyapunov/halo orbit and the southern 9:2 resonant NRHO intended for the Gateway mission, as highlighted in red in Fig. 3, with initial conditions summarized in Table 1.

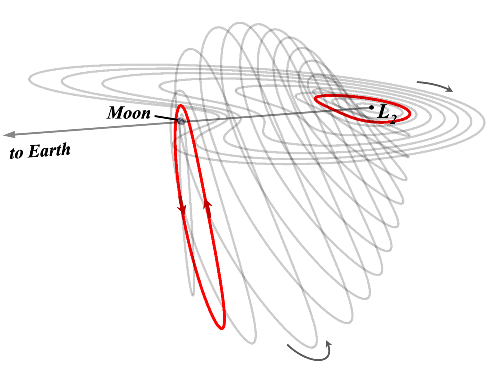

Fig. 3: L_2 Lyapunov and halo orbit family members, with the bifurcating L_2 Lyapunov/halo orbit and southern 9:2 resonant NRHO indicated in red.

Table 1: Orbit Initial Conditions

	L2 Bifurcating Orbit	**9:2 Resonant NRHO [20]**
Position	[1.1808777, 0, 0] nd = [454340.3, 0, 0] km	[1.0218727, 0, -0.1819940] nd = [393163.5, 0, -70021.8] km
Velocity	[0, -0.1557031, 0] nd = [0, -0.159453, 0] km/s	[0, -0.1029320, 0] nd = [0, -0.105411, 0] km/s
Period	3.4154 nd = 14.85 days	1.5091 nd = 6.56 days
JC	3.1522 nd	3.0466 nd

In this analysis, 998 constant Δv perturbations are applied isotropically as a Monte Carlo simulation at 50 equidistant locations around each of the selected orbits, correlating to potential orbital departure maneuvers in any direction away from the initial orbital state. The Δv directions are selected to ensure a deterministic and evenly spaced spherical distribution according to Deserno's regular placement method [7]. Given the nature of the distribution method, the number of desired directions does not necessarily equal the number of generated directions, explaining the atypical choice of 998 directions instead of a cleaner 1000. Two constant Δv magnitudes are considered: (a) 0.05 km/s, corresponding to the order of magnitude of average velocity perturbation quantities of debris objects resulting from on-orbit explosion of a 500 kg spacecraft [5], and (b) 0.5 km/s, which is on the order of magnitude of a spacecraft maneuver to travel from L_2 to a low lunar orbit (LLO) [8]. All trajectories in this study are propagated for 30 days using the Earth-Moon CR3BP model with stopping conditions at the Moon's surface and 120 km above Earth's surface. A trajectory is considered to have left the Earth-Moon sphere of influence (SOI) at a distance of 2.415 nd = 9.2918e5 km from the Barycenter, where the SOI radius is calculated from the distance d between the Barycenter and the Sun, and the masses of the Earth m_e, Moon m_m, and Sun m_s, by $r_{SOI} = d \cdot (\frac{m_e+m_m}{m_s})^{2/5}$ [23]. For the purposes of this investigation, a spacecraft within 10,000 km (0.026 nd) of its orbit of origination is considered to be within the *orbital vicinity*. The 50 equidistant orbit locations are distinguished and colored according to arc angle θ, as shown in Fig. 4. For the L_2 bifurcating orbit, arc angle is defined as the angle relative to the L_2 origin and the negative x-axis, such that $\theta = \tan^{-1}(y/\text{-}x)$. For the NRHO orbit, arc angle is taken as the orbital eccentric anomaly which represents the angle between the perilune and the orbit location, relative to the center of the orbit. Given that the NRHO orbit is highly eccentric, eccentric anomaly is preferable to true anomaly for obtaining an even distribution of angles and color discretization, as it is measured relative to orbit center rather than the Moon. Hereafter, the eccentric anomaly angle for the NRHO scenario will be referred to as the arc angle. Note that for the bifurcating orbit, 0°and 360°represent a location with x less than that of L_2 and $y = 0$, while 180°represents a location with x greater than that of L_2 and $y = 0$. For the NRHO, 0°and 360°represent the location of perilune, while 180°represents apolune.

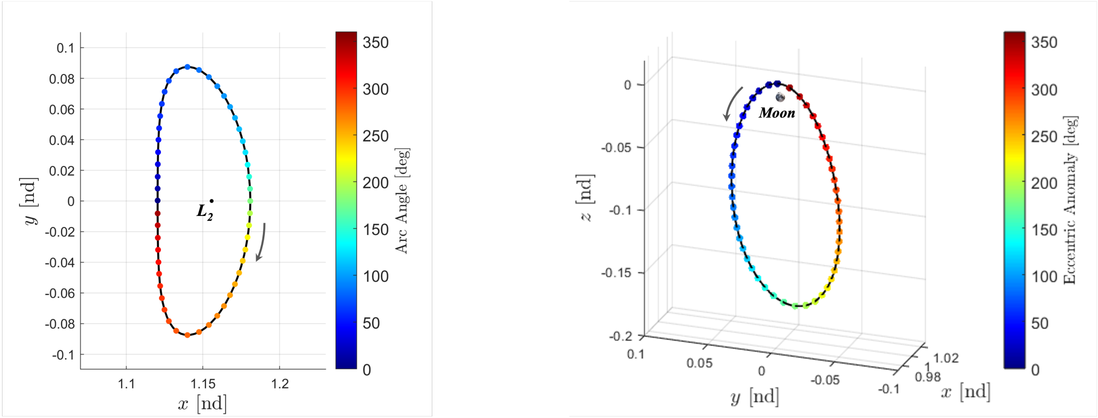

(a) Bifurcating L_2 Lyapunov/halo orbit.

(b) Southern 9:2 synodic resonant NRHO.

Fig. 4: 50 equidistant maneuver locations around each orbit of interest, colored according to arc angle. The arrow denotes direction of natural motion around the orbit.

For the surveillance of both the bifurcating L_2 Lyapunov/halo orbit and Southern 9:2 synodic resonant NRHO, the object parameters are listed in Table 2. The initial angles with respect to the Sun and the Moon are assumed to be zero degrees. An additional test case with a different Sun and Moon angle of 180°and 90°, respectively, is presented at the end of the investigation.

Table 2: Selected object parameters for all simulations using the reflection model from equation.

Object radius	1 meter
Lambertian reflection coefficient	0.5

For evaluating the overall visibility, four constraints mentioned in Section 3 are applied to all the cases and are shown in Table 3.

Table 3: Applied constraints for BCR4BP approximated modeling simulations.

Constraint	Limit
Limiting magnitude	18
Sun exclusion angle	30°
Moon exclusion angle	10°
Earth exclusion angle	15°

5.2 L_2 Bifurcating Orbit: Search Space Characterization

Velocity perturbations of 0.05 km/s and 0.5 km/s are considered in 998 uniformly spaced directions at 50 equidistant locations around a planar L_2 libration point orbit belonging to both the Lyapunov and halo orbit families. The perturbations represent possible spacecraft maneuvers away from the orbit, and an assessment of surveillance capability in detecting the spacecraft over the entire propagation period is performed. Figs. 5 and 6 show the position of every object from all 50 orbit locations for the two Δv cases, after a given propagation time, colored according to discrete elapsed times.

For a maneuver with Δv magnitude of 0.05 km/s, Fig. 5 reveals that objects move slowly away from the original orbit, remaining within the vicinity for the first few days, dissipating to less than 15% after 10 days, and leaving the region almost entirely at 30 days post maneuver, with over half of objects departing the Earth-Moon SOI. Around 13.82% of objects over all maneuver possibilities impact the Moon. The objects have a mean Jacobi constant energy of 3.1498, which is similar to but marginally more energetic than that of the originating orbit, $JC = 3.1522$, and below that of the L_2 libration point. The objects have a limited JC range of 0.0343. The small object energies are apparent in Fig. 5(a), in which the object trajectories are heavily planar and remain close together over time. For a larger, more costly maneuver of 0.5 km/s Δv, objects are ejected much faster and farther, as anticipated, with only 4.2% of all objects remaining in the orbital vicinity after just one day, and merely 0.1% of objects lingering after 10 days until the end of the propagation period. As in the lower Δv case, over half of objects exit the Earth-Moon SOI over the course of propagation, and only 1.18% of all possible objects result in lunar impact. Neither case yields Earth impacts or near misses. The mean object Jacobi constant is 2.9138, indicating a larger energy than that of the original orbit, and large

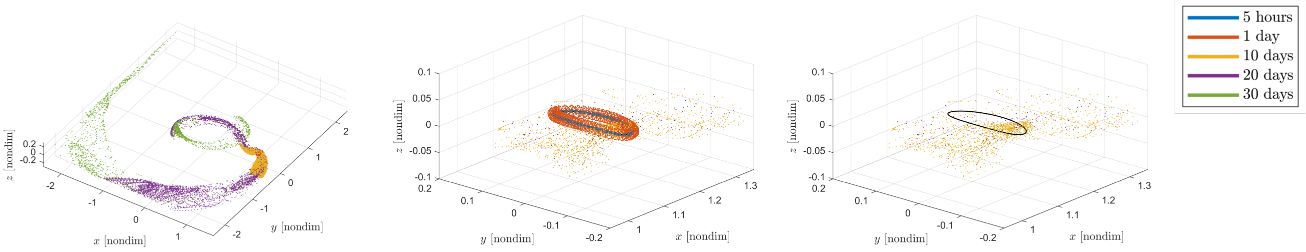

(a) (b) (c)

Fig. 5: Locations of spacecraft subject to a 0.05 km/s Δv maneuver after elapsed times of 5 hours (blue), 1 day (orange), 10 days (yellow), 20 days (purple), and 30 days (green). (a) Location of all objects within Earth-Moon SOI. (b) Location of objects nearby the original L_2 orbit. (c) Location of objects nearby the original L_2 orbit for elapsed times of 10, 20, and 30 days.

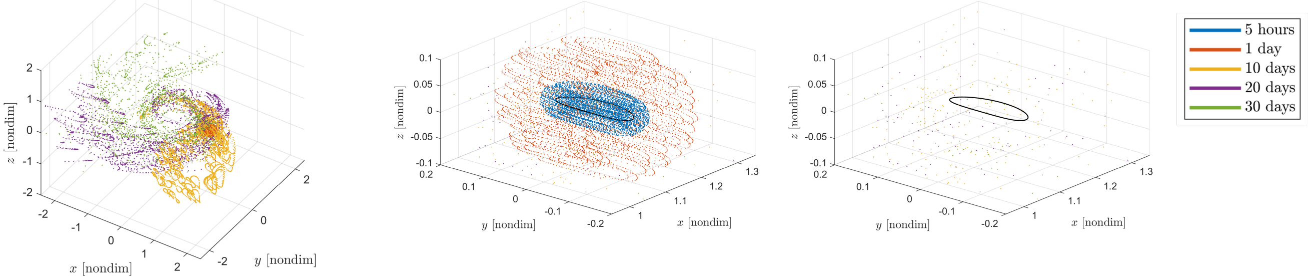

(a) (b) (c)

Fig. 6: Locations of spacecraft subject to a 0.5 km/s Δv maneuver after elapsed times of 5 hours (blue), 1 day (orange), 10 days (yellow), 20 days (purple), and 30 days (green). (a) Location of all objects within Earth-Moon SOI. (b) Location of objects nearby the original L_2 orbit. (c) Location of objects nearby the original L_2 orbit for elapsed times of 10, 20, and 30 days.

enough that many trajectories are not bounded by ZVCs in the x-y plane. The JC range is higher than that of the 0.05 km/s case, with a value of 0.3429. In fact, the JC range ΔJC is found to be proportional to the associated Δv magnitude such that $\Delta JC = 4\,v_0\,\Delta v$, where v_0 is the magnitude of the initial orbital velocity [5]. Therefore, given the same initial velocity, the JC range for objects perturbed by 0.5 km/s is always an order of magnitude greater than for a 0.05 km/s perturbation. Table 4 offers a summary of statistics for both Δv scenarios.

Table 4: Percentage of objects that impact the Moon or Earth, exit the Earth-Moon SOI, and remain in the L_2 orbit vicinity after a given elapsed propagation time.

				Remain in L_2 orbit vicinity				
Δv	**Lunar Impacts**	**Earth Impacts**	**Exit EM SOI**	**5 hrs**	**1 dy**	**10 dys**	**20 dys**	**30 dys**
0.05 km/s	13.82%	0.00%	55.27%	100%	100%	14.41%	1.32%	.25%
0.5 km/s	1.18%	0.00%	57.52%	92.92%	4.20%	0.12%	0.09%	0.10%

Poincaré maps enable a deeper examination of the extensive design space of the CR3BP, by reducing the dimension of the state space. While these maps are often used for transfer design to locate favorable transits between regions in cislunar space [25], in this work they are used more simply to determine patterns in trajectory behavior and identify the significance of changes in initial state. A hyperplane is placed at a location on the x-axis central to the Earth-Moon cislunar region of interest, between the Earth and the L_2 Lagrange point (x = 0.5718 nd). Figs. 7 and 8 represent double-sided hyperplane crossings of all 50×998 trajectories with Δv magnitudes of 0.05 km/s and 0.5 km/s, respectively. The maps are colored according to the orbital arc angle from which the trajectories emanated, and 3-dimensional representations are provided to further clarify the impact of arc angle.

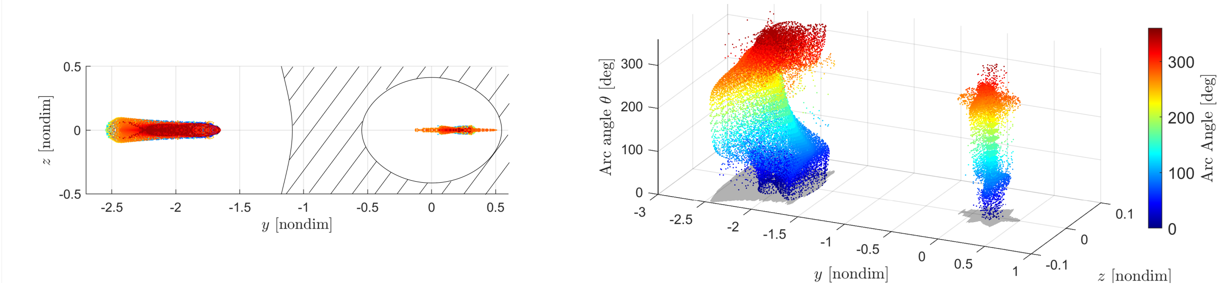

(a) y-z Poincaré map with ZVC for $JC = 3.1326$.

(b) y-z Poincaré map plotted relative to arc angle.

Fig. 7: Poincaré map intersection of objects subject to a Δv maneuver with 0.05 km/s magnitude from a planar L_2 orbit of $JC = 3.1522$, coloured according to the orbital arc angle θ from which the objects originated. Hyperplane located at $x = 0.5718$ nd. Hatched area delineates forbidden region. Note that the x and y axes in (b) are not equal.

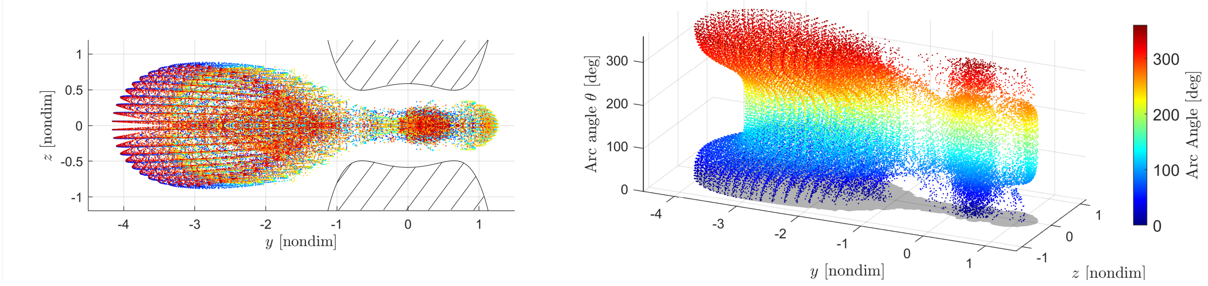

(a) y-z Poincaré map with ZVC for $JC = 2.7423$.

(b) y-z Poincaré map plotted relative to arc angle.

Fig. 8: Poincaré map intersection of objects subject to a Δv maneuver with 0.5 km/s magnitude from a planar L_2 orbit of $JC = 3.1522$, coloured according to the orbital arc angle θ from which the objects originated. Hyperplane located at $x = 0.5718$ nd. Hatched area delineates forbidden region.

Both figures reveal the emergence of bounded natural structures, symmetric about the y-axis, indicating that the orbital trajectories are not entirely random. The maps of trajectories with a perturbation of 0.05 km/s, displayed in Fig. 7, show two distinct regions of map crossings, signifying the presence of forbidden regions, such that the leftmost trajectories are those that have traveled outside of the ZVC, away from the Moon and Earth, in the negative y-direction, while the rightmost trajectories travel towards the Moon and Earth in the positive y-direction and are trapped within the ZVC. The ZVC contour for the highest energy (lowest JC) object is illustrated in black in Fig. 7(a), and it is clear that the trajectories are not solely constrained by the ZVCs. The trajectories are highly planar and are indeed influenced by the location of the applied perturbation around the orbit, such that objects departing from a part of the orbit with a positive initial $\dot{y}$, between arc angles of around 275°to 90°, spread farther than those from locations with negative initial $\dot{y}$. The total cross-sectional area covered by all trajectories is 0.149 nd^2 (2.21e10 km^2), while the area of objects trapped inside the ZVC alone is 0.023 nd^2 (3.46e9 km^2). Fig. 8 lacks a gap in y-coordinates, signifying that many trajectories are not impeded by ZVCs in the x-y rotating plane, although out-of-plane boundaries exist, as shown by the ZVC in Fig. 8(a) for the trajectory with the lowest JC of 2.7423. This case reveals an even more stark impact of arc angle, whereby the area of travel remains nearly constant, but the location is shifted in the positive y-direction for trajectories emanating from locations with negative initial $\dot{y}$. The total cross-sectional area covered by all trajectories is 5.679 nd^2 (8.407e11 km^2), which is over 38 times larger than the possible area traveled by trajectories subject to a 0.05 km/s velocity perturbation, creating a much more complex surveillance challenge. The Poincaré maps assist in narrowing the search space and provide predictive insight into the behaviour of objects in the CR3BP subject to varying maneuver magnitudes and locations.

5.3 L_2 Bifurcating Orbit: Surveillance Investigation

The bifurcating L_2 Lyapunov/halo orbit with 0.05 km/s and 0.5 km/s Δv perturbations in 998 uniformly spaced directions at 50 equidistant locations is then analyzed for optimal average visibility offered by the application of BCR4BP parameterization and PSO.

For both of the L_2 orbits with 0.05 km/s and 0.5 km/s, the perturbed orbits are mapped onto a pre-selected points in the Earth-Moon rotating plane, which are equally spaced within the sphere of influence of the Earth. These pre-selected points serve as the observers and the mapped points serve as the objects.

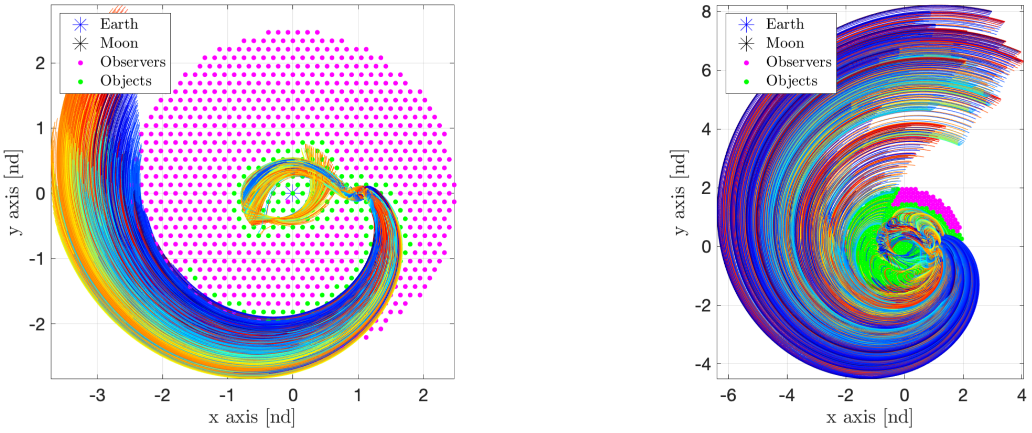

(a) 0.05 km/s Δv

(b) 0.5 km/s Δv

Fig. 9: Mapped planar points for perturbed L_2 bifurcating orbits with Δv maneuvers of 0.05 km/s and 0.5 km/s.

Fig. 9 illustrates the planar mapped objects along with observers for a bifurcating L_2 Lyapunov/halo orbit with 0.05 km/s and 0.5 km/s Δv perturbations. The x-axis and y-axis represent the coordinate axes for the non-dimensional Earth-Moon rotating frame. The position of the Moon and the Earth are shown in black and blue star, respectively. The equally spaced magenta points represent all the observers and the green points represent all the mapped objects spanned by these perturbed orbits in the radius of the influence of the Earth. Fig. 9a and 9b illustrates the mapped objects for 0.05 km/s Δv and 0.5 km/s Δv perturbations, respectively. These mapped locations are utilized to evaluate average visibility, which is further employed to obtain optimal observers through PSO.

5.3.1 L_2 bifurcating orbit with 0.05 km/s Δv, $\phi_0 = 0$ and $\theta_0 = 0$

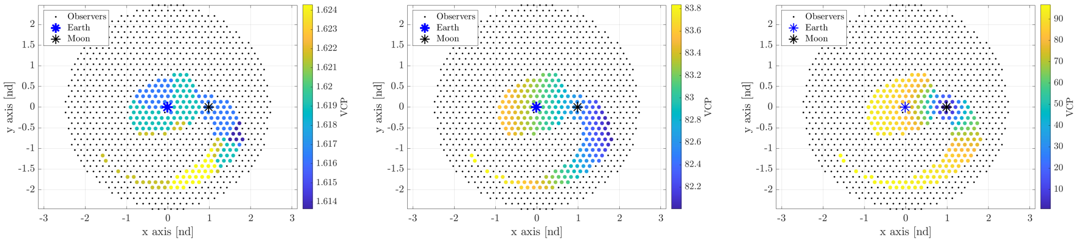

(a) Magnitude constraint (b) Sun exclusion angle constraint (c) Moon exclusion angle constraint

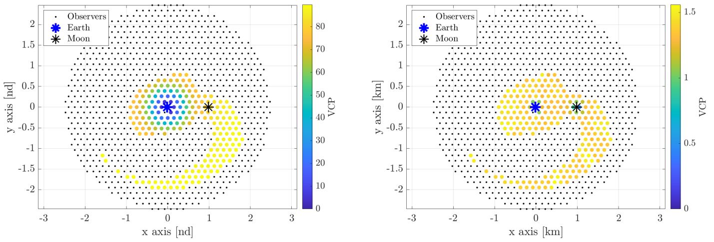

(d) Earth exclusion angle constraint (e) All constraints

Fig. 10: VCP_{all} plots for mapped objects in the L_2 bifurcating orbit with 0.05 km/s Δv for 30 days.

In Fig. 10, the average visibility using VCP_{all} is evaluated for all constraints individually and together for a bifurcating L_2 Lyapunov/halo orbit with 0.05 km/s Δv for 30 days. The x-axis and y-axis are same as the axes in Fig. 9. The colorbar provides the VCP_{all} using the magnitude constraint, Sun exclusion angle constraint, Moon exclusion angle constraint, Earth exclusion angle constraint and all of them combined in Fig. 10a (a), 10a (b), 10a (c), 10a (d), and 10a (e), respectively. The VCP_{all} due to magnitude constraint has low values due to larger distances between the object and the observer and thus significantly affects the visibility due to all constraints. The object with higher invisibility due to the Earth and the Moon exclusion angle constraints remains confined to a region as Earth and Moon are fixed in the Earth-Moon rotating frame at all times. The orbit of the Sun completes more than one full period in 30 days and hence has a larger region of low VCP due to the overlap in its position.

The visibility maps produced in the Fig. 10 are utilized to produce optimal observers in Fig. 11. Fig. 11 illustrates the location of optimal observers that can view the maximum number of objects when constrained with the combined VCP from all observers greater than 0 percent using particle swarm optimization for a bifurcating L_2 Lyapunov/halo orbit with 0.05 km/s Δv. The predefined set of locations serve as observers and the mapped locations serve as objects which the optimization utilizes for fulfilling the visibility requirement. The x-axis and y-axis represent the axes associated with the non-dimensional Earth-Moon rotating frame. The location of the Earth and the Moon as same as depicted in the Fig. 10. The colorbar represents the sum of the VCP_{single} from all the optimal observers for mapped object locations. Fig. 11a has optimal visibility when 2 observers are surveilling the region. Similarly, Fig. 11b has 4 observers, Fig. 11c has 6 observers, Fig. 11d has 8 observers, and Fig. 11e has 10 observers for maximizing the visibility coverage from them. As the number of observers increases, the number of objects satisfying the combined VCP > 0 percent also increases.

5.3.2 L_2 bifurcating orbit with 0.5 km/s Δv, $\phi_0 = 0$ and $\theta_0 = 0$

Similar to Fig. 11, optimized cumulative VCP plots for a bifurcating L_2 Lyapunov/halo orbit with 0.5 km/s Δv are illustrated in Fig. 12. The axis, object parameters, visibility constraints and optimization constraints are consistent with Fig. 11. The color bar indicates the sum of VCP_{single} across all optimal observers for the mapped object locations. Fig. 12a shows optimal visibility with 2 observers, Fig. 12b with 4, Fig. 12c with 6, Fig. 12d with 8, and Fig. 12e with 10 observers. As the number of observers increases, the number of objects satisfying the combined VCP greater

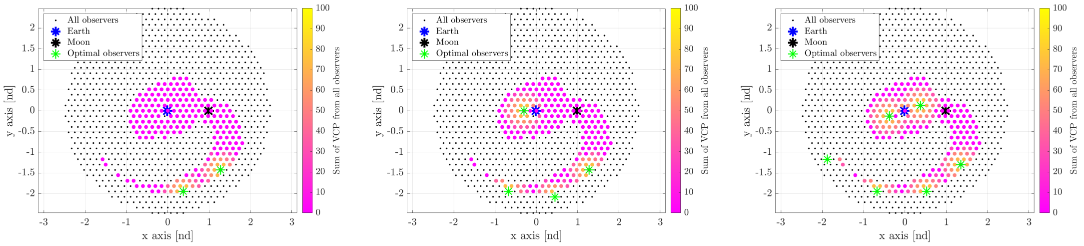

(a) 2 observers (b) 4 observers (c) 6 observers

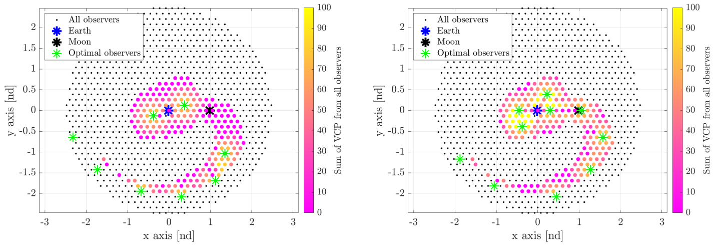

(d) 8 observers (e) 10 observers

Fig. 11: Optimized cumulative VCP plots for the L_2 bifurcating orbit with 0.05 km/s Δv when observed from (a) 2 observers, (b) 4 observers, (c) 6 observers, (d) 8 observers, (e) 10 observers.

than 0 percent also rises.

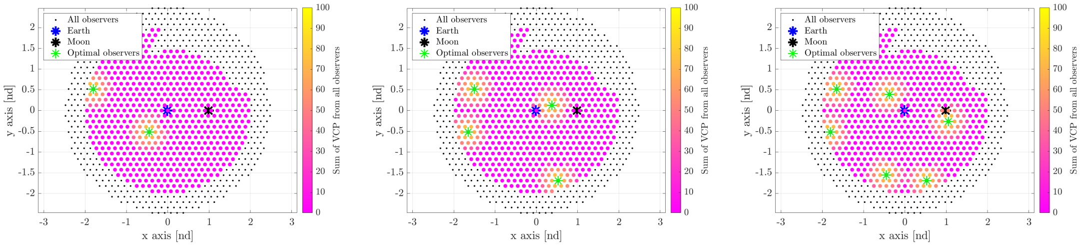

(a) 2 observers (b) 4 observers (c) 6 observers

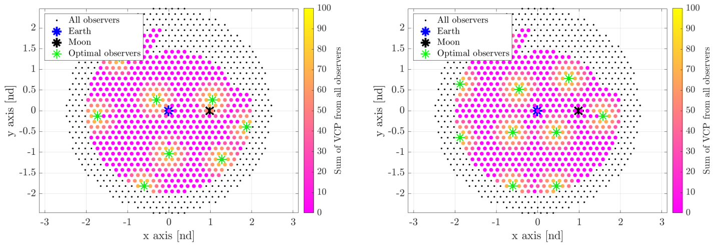

(d) 8 observers (e) 10 observers

Fig. 12: Optimized cumulative VCP plots for the L_2 bifurcating orbit with 0.5 km/s Δv when observed from (a) 2 observers, (b) 4 observers, (c) 6 observers, (d) 8 observers, (e) 10 observers.

5.4 Near Rectilinear Halo Orbit: Search Space Characterization

Velocity perturbations of 0.05 km/s and 0.5 km/s are considered in 998 uniformly spaced directions at 50 equidistant locations around the southern 9:2 resonant L_2 NRHO. Figs. 13 and 14 show the position states of every object from all 50 orbit locations for the 0.05 km/s and 0.5 km/s Δv cases, respectfully, after a given propagation time, colored according to elapsed time.

For a maneuver magnitude of 0.05 km/s, most objects linger in the vicinity of the NRHO for the first few days, slowly expanding away from the orbit, with about a third of objects remaining after 10 days, and a little over 2% persisting after the full 30 day propagation period. Close to a third of objects impact the Moon at some point during the propagation, while only around 9% escape the Earth-Moon SOI. Nearly all lunar impacts occurred within 10 days of the maneuver. The objects retain a mean Jacobi constant energy of 3.0443, which aligns closely with that of the originating orbit, and indicates that both the L_1 and L_2 libration point regions are accessible for travel, while L_3 remains forbidden. The objects have a *JC* range of 0.3259, an order of magnitude larger than that of the earlier planar L_2 orbit investigation. For a much larger maneuver magnitude of 0.5 km/s, it is unsurprising that objects spread away from the NRHO farther and faster than the previous scenario, as shown in Fig. 14. After only one day, over 80% of objects have left the orbital vicinity, while the rate of object flux away from the orbit slows after 10 days. Interestingly, the number of objects in the NRHO vicinity increases slightly between elapsed times of 20 and 30 days. Here, we are likely witnessing objects that have traveled around the Earth returning to the region. Many fewer objects impact the Moon, while over a third of spacecraft exit the Earth-Moon SOI over the propagation duration. The majority of lunar impacts occurred in less than two days post-maneuver. Neither scenario results in Earth impacts. The mean object *JC*

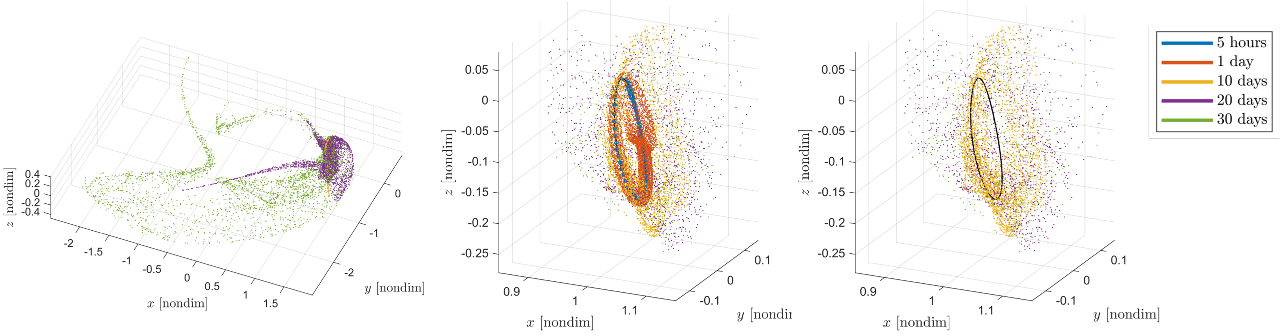

(a) (b) (c)

Fig. 13: Locations of spacecraft subject to a 0.05 km/s Δv maneuver after elapsed times of 5 hours (blue), 1 day (orange), 10 days (yellow), 20 days (purple), and 30 days (green). (a) Location of all objects. (b) Location of objects nearby the original NRHO. (c) Location of objects nearby the original NRHO for elapsed times of 10, 20, and 30 days.

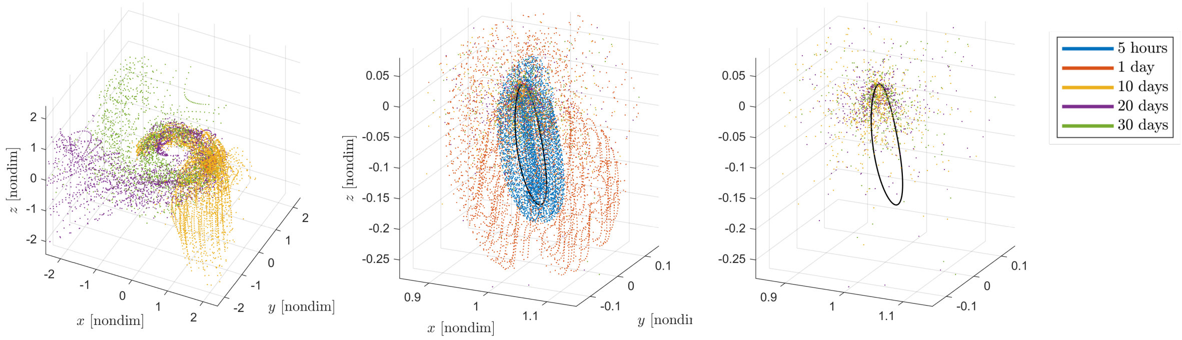

(a) (b) (c)

Fig. 14: Locations of spacecraft subject to a 0.5 km/s Δv maneuver after elapsed times of 5 hours (blue), 1 day (orange), 10 days (yellow), 20 days (purple), and 30 days (green). (a) Location of all objects within the Earth-Moon SOI. (b) Location of objects nearby the original NRHO. (c) Location of objects nearby the original NRHO for elapsed times of 10, 20, and 30 days.

is 2.8083, enabling unrestricted travel in the x-y plane, while the JC varies widely with a range of 3.2586, indicating large variability in object motion. Table 5 provides the complete statistics for both maneuver magnitudes.

Table 5: Percentage of objects that impact the Moon or Earth, exit the Earth-Moon SOI, and remain in the NRHO vicinity after a given elapsed propagation time.

				Remain in NRHO vicinity				
Δv	**Impact Moon**	**Impact Earth**	**Exit EM SOI**	**5 hrs**	**1 dy**	**10 dys**	**20 dys**	**30 dys**
0.05 km/s	31.60%	0.00%	9.16%	100%	97.81%	36.37%	10.05%	2.56%
0.5 km/s	7.64%	0.00%	37.07%	94.75%	17.13%	8.10%	6.54%	6.80%

A hyperplane is placed at a location on the x-axis halfway between the Earth and the L_2 Lagrange point (x = 0.5718 nd). Figs. 15 and 16 represent double-sided hyperplane crossings of each trajectory subject to initial Δv magnitudes of 0.05 km/s and 0.5 km/s, respectively. The maps are colored according to the orbital arc angle from which the trajectories emanated, and 3-dimensional representations are provided to further clarify the impact of arc angle. The maps additionally display ZVCs for the most energetic (lowest JC) objects, which serve as the minimum boundary for all objects. Similarly to the planar L_2 orbit, both NRHO maps indicate the existence of bounded natural structures, although they no longer display symmetry about the y-axis. Additionally, the arc angle has a larger impact than simply shifting the departure tube along the y-axis. In the case of the 0.05 km/s Δv magnitude, two clusters are apparent in Fig. 15. The first cluster represents the 4% of objects that depart the orbit in the positive y-direction, heading towards the Earth, in what could be considered inside a respective ZVC, while the second, larger cluster represents the 96% of trajectories that depart in the negative y-direction, traveling around any ZVCs. The first cluster is tightly packed, while the structure of the second cluster is hollow, as if the objects are traveling along the surface of the departure tube, and not through it – akin to periodic orbit invariant manifold structures. Objects emanating at arc angles near perilune, between about -80°to +80°, do not ever depart the NRHO vicinity with positive y-velocities, and thus do not comprise any of the smaller cluster. They do, however, appear to cover more area in the cislunar region outside of the ZVC, traveling along the surface of a departure tube that is skewed towards the positive y-z direction. Trajectories from the other departure locations do not form a closed surface. The total cross-sectional area covered by all trajectories is 0.605 nd^2 (8.95e10 km^2), while the area of objects that have traveled inside the ZVC towards the Earth is 0.042 nd^2 (6.17e9 km^2). This region of travel is almost double that of the bifurcating orbit investigation. The findings for the 0.5 km/s Δv magnitude are exceedingly different. The objects have larger energies and are thus much less constrained by forbidden regions, resulting in a merging of the clusters that appeared in Fig. 15. Once again, the objects emanating within 60°to 80°of perilune travel the farthest distances, which is in line with the fact that objects at periapsis possess the largest speeds. Trajectories from arc angles around 90°to 275°appear to occupy similar shaped and sized areas, shifted along the z-axis. Those areas then look to be smeared out of proportion for angles near perilune. The total cross-sectional area covered by all trajectories is 17.165 nd^2 (2.54e12 km^2), a vast region – over three times that of the

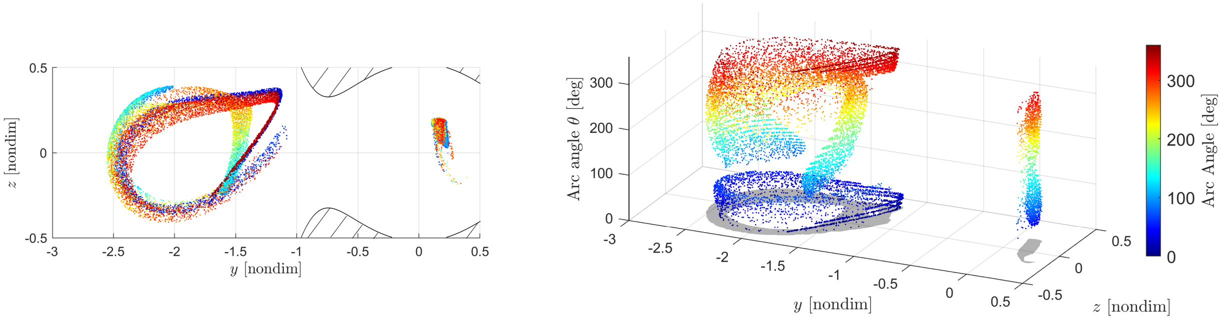

(a) y-z Poincaré map with ZVC for $JC = 2.8813$.

(b) y-z Poincaré map plotted relative to arc angle.

Fig. 15: Poincaré map intersection of objects subject to a Δv maneuver with 0.05 km/s magnitude from a 9:2 resonance NRHO orbit of $JC = 3.0466$, coloured according to the orbital arc angle θ from which the objects originated. Hyperplane located at $x = 0.5718$ nd. Hatched area delineates the forbidden region.

bifurcating orbit case – that extends far beyond the Earth-Moon SOI. While 0.5 km/s is a costly maneuver, it affords the opportunity for an object deploying from a 9:2 NRHO (especially near perilune) to travel virtually anywhere in cislunar space. This will require incredible future surveillance capability.

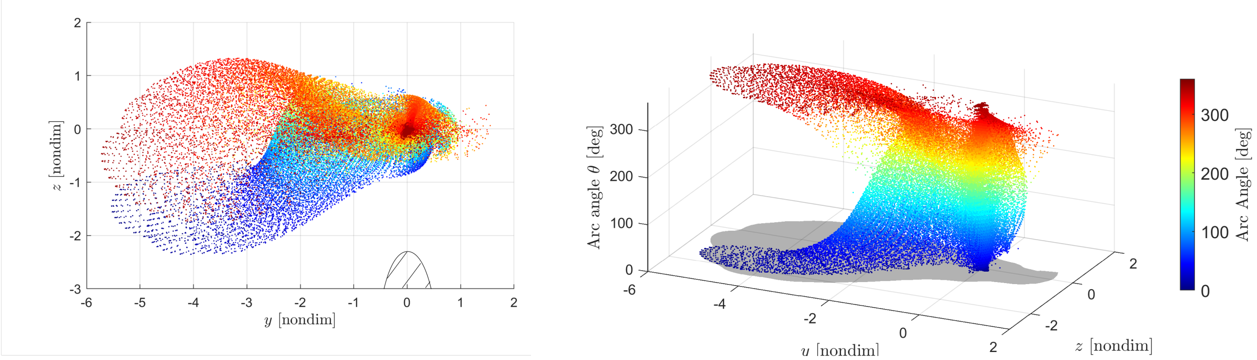

(a) y-z Poincaré map with ZVC for $JC = 1.1789$.

(b) y-z Poincaré map plotted relative to arc angle.

Fig. 16: Poincaré map intersection of objects subject to a Δv maneuver with 0.5 km/s magnitude from a 9:2 resonance NRHO orbit of $JC = 3.0466$, coloured according to the orbital arc angle θ from which the objects originated. Hyperplane located at $x = 0.5718$ nd. Hatched area delineates the forbidden region.

5.4.1 Near Rectilinear Halo Orbit: Surveillance Investigation

For both NRHO orbits with 0.05 km/s and 0.5 km/s perturbations, the perturbed orbits are mapped onto pre-selected, equally spaced points within the Earth's radius of influence, similar to the L_2 Halo orbit setup. The object parameters and optimization constraints are consistent with those used for the L_2 Halo orbit (see Table 2 and 3). Fig. 17 shows the planar mapped objects and observers for NRHO orbits with 0.05 km/s and 0.5 km/s perturbations. The x-axis and y-axis are aligned with the Earth-Moon rotating frame, with the Moon and Earth marked in black and blue, respectively. Magenta points denote observers, and green points indicate mapped objects within Earth's influence. Figs. 17a and 17b depict mapped objects for 0.05 km/s and 0.5 km/s perturbations, respectively, which are used to calculate average visibility and determine optimal observers through PSO. The initial angles relative to the Sun and the Moon are assumed to be zero in Fig. 18 and 19 but in Fig. 20, the angles with the Sun and the Moon are taken to be 180°and 90°.

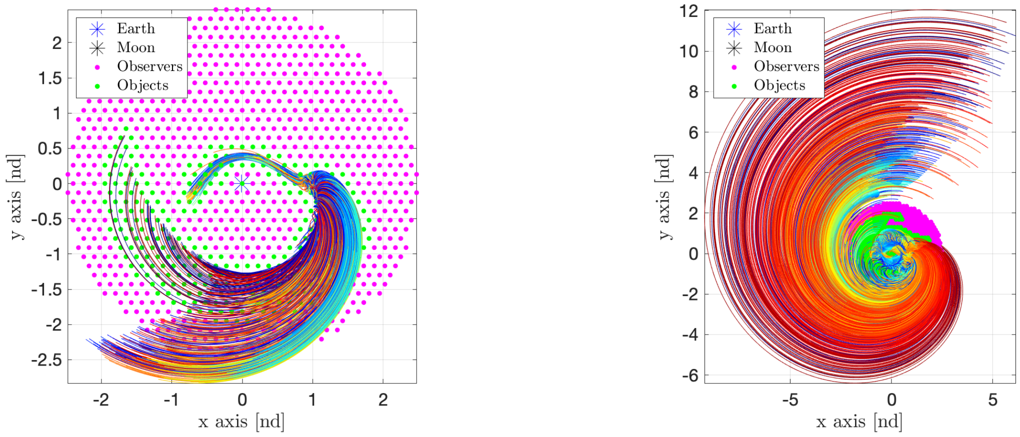

(a) 0.05 km/s

(b) 0.5 km/s

Fig. 17: Mapped planar points for perturbed NRHO orbits with 0.05 km/s and 0.5 km/s Δv

5.4.2 NRHO with 0.05 km/s Δv, $\phi_0 = 0$ and $\theta_0 = 0$

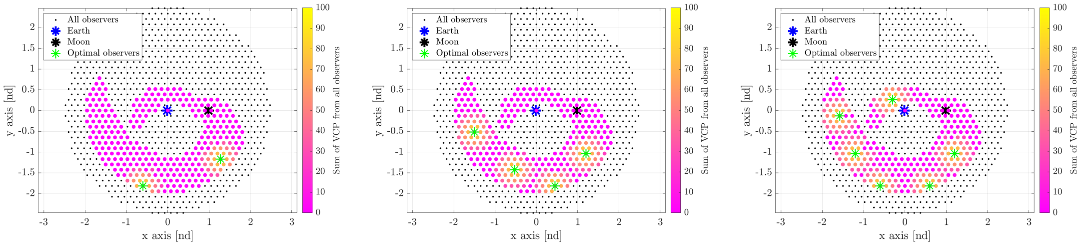

(a) 2 observers (b) 4 observers (c) 6 observers

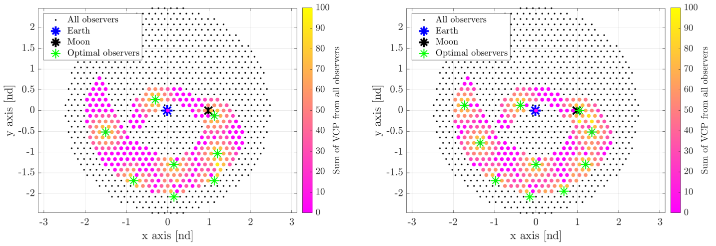

(d) 8 observers (e) 10 observers

Fig. 18: Optimized cumulative VCP plots for NRHO orbit with 0.05 km/s Δv when observed from (a) 2 observers, (b) 4 observers, (c) 6 observers, (d) 8 observers, (e) 10 observers.

Fig. 18 provides optimal visibility maps for the NRHO with 0.05 km/s Δv perturbations. This figure illustrates observer positions that maximize the number of visible objects using particle swarm optimization. The predefined observer locations and mapped object locations from Fig. 17a are used to meet visibility requirements. The x-axis and y-axis align with the Earth-Moon rotating frame, with Earth and the Moon positioned as in Fig. 17. The colorbar shows the sum of VCP_{single} for the optimal observers. Figs. 18a through 18e display configurations with 2, 4, 6, 8, and 10 observers, respectively. Increasing the number of observers improves the coverage, increasing the number of visible objects with VCP greater than 0 percent.

5.4.3 NRHO with 0.5 km/s Δv, $\phi_0 = 0$ and $\theta_0 = 0$

Fig. 19 shows optimal visibility maps for the NRHO with 0.5 km/s Δv perturbations, highlighting observer positions that maximize visible objects using particle swarm optimization. Observer and object locations from Fig. 17b are used. The x and y axes align with the Earth-Moon rotating frame, and the colorbar represents the total VCP_{single} for optimal observers. Figs. 19a to 19e display results for 2, 4, 6, 8, and 10 optimal observers, respectively, with increased visible objects improving visibility coverage.

5.4.4 NRHO with 0.5 km/s Δv, $\phi_0 = 180^\circ$ and $\theta_0 = 90^\circ$

Figure 20 displays optimal visibility maps for the NRHO with 0.5 km/s Δv perturbations for $\phi_0 = 180^\circ$ and $\theta_0 = 90^\circ$. All the axes, along with the Earth and the Moon, are the same as described in Fig. 19. As the initial positions of the Sun and the Moon have shifted, the optimal observers also shift to account for invisibilities coming from the Sun and Moon.

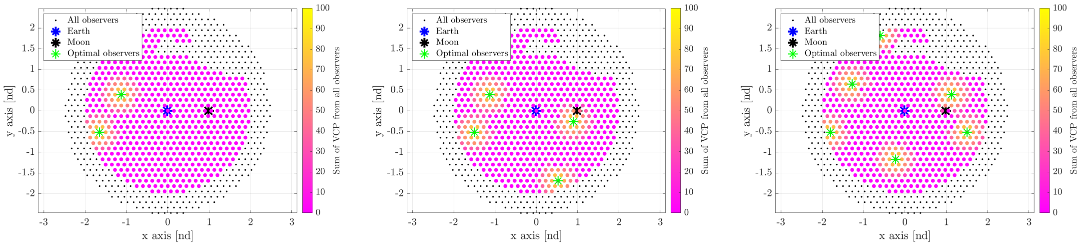

(a) 2 observers (b) 4 observers (c) 6 observers

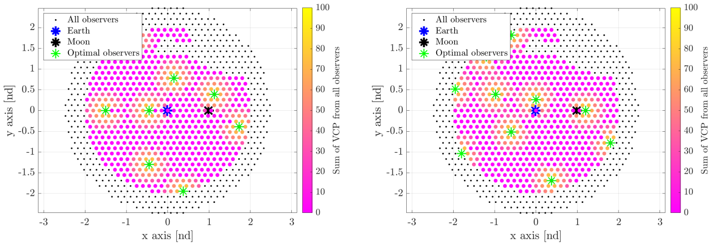

(d) 8 observers (e) 10 observers

Fig. 19: Optimized cumulative *VCP* plots for NRHO orbit with 0.5 km/s Δv when observed from (a) 2 observers, (b) 4 observers, (c) 6 observers, (d) 8 observers, (e) 10 observers with $\phi_0 = 0°$ and $\theta_0 = 0°$

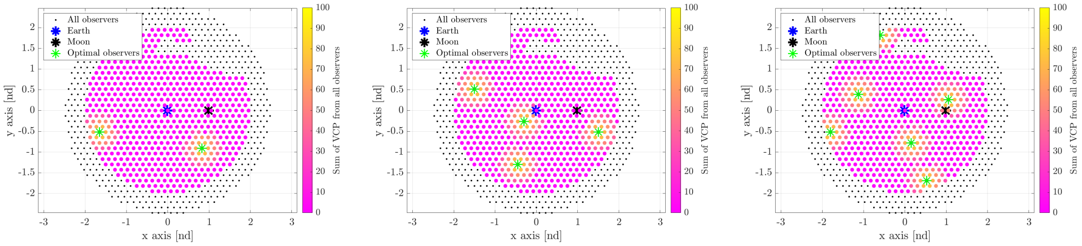

(a) 2 observers (b) 4 observers (c) 6 observers

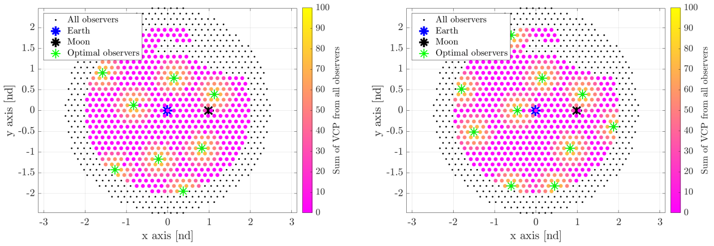

(d) 8 observers (e) 10 observers

Fig. 20: Optimized cumulative *VCP* plots for NRHO orbit with 0.5 km/s Δv when observed from (a) 2 observers, (b) 4 observers, (c) 6 observers, (d) 8 observers, (e) 10 observers with $\phi_0 = 180°$ and $\theta_0 = 90°$.

5.4.5 NRHO with 0.5 km/s Δv with mapped points in 3D

Since the perturbed orbits span in space, in this paper, NRHO orbit wil 0.5 km/s Δv has been investigated in a three-dimensional space. Fig. 21 illustrates the mapped objects and predefined observers in three dimensional space for the NRHO with 0.5 km/s Δv. In the Fig. 21, the pre-selected observers lie within the radius of the influence of the Earth in the x-y plane and range from -1 to 1 nd units in z-direction. The observers in the z-axis are restricted within the mentioned range as perturbed orbits do not span out of this and farther observers will have difficulty in viewing the object due to magnitude constraint.

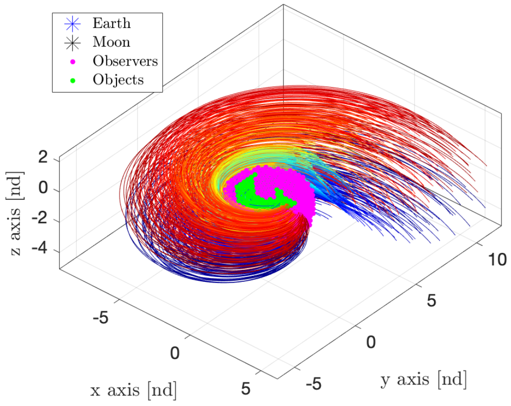

(a) 0.5 km/s

Fig. 21: Mapped 3D points for perturbed NRHO orbits with 0.5 km/s Δv

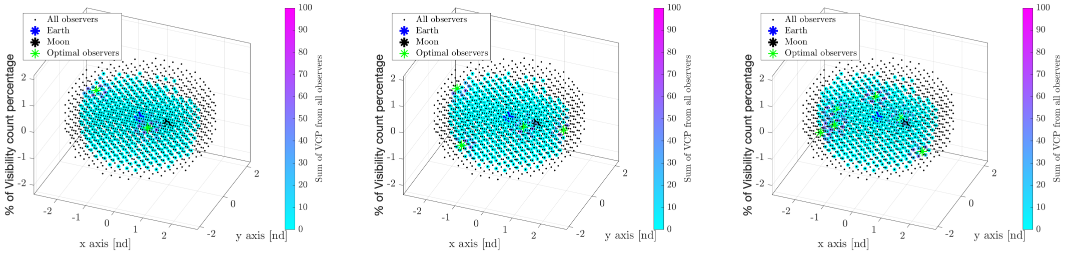

(a) 2 observers

(b) 4 observers

(c) 6 observers

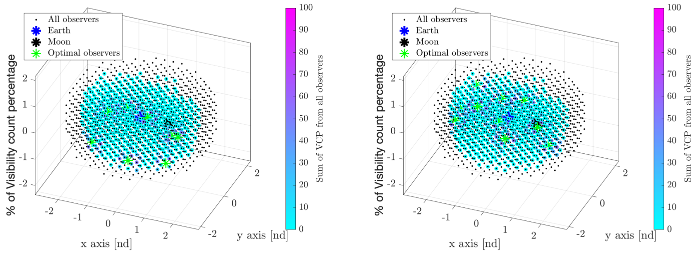

(d) 8 observers

(e) 10 observers

Fig. 22: Optimized cumulative VCP plots for NRHO orbit with 0.5 km/s Δv when observed from (a) 2 observers, (b) 4 observers, (c) 6 observers, (d) 8 observers, (e) 10 observers.

Figure 22 presents three-dimensional optimal visibility maps for the NRHO with 0.5 km/s Δv perturbations, illustrating observer positions that maximize the number of visible objects using particle swarm optimization. The observer and object locations from Figure 21 are employed to meet visibility criteria. The x and y axes correspond to the Earth-Moon rotating frame, with the Earth and Moon positioned as shown in Figure 21. The colorbar represents the total sum of VCP from all the optimal observers. Figures 22a through 22e depict configurations with 2, 4, 6, 8, and 10 observers, respectively, where increasing the number of observers enhances coverage and the number of visible objects.

6. CONCLUSIONS

The rate of growth of current and planned cislunar missions demands commensurate surveillance capability, to ensure secure and reliable space domain awareness in the region. Existing ground-based surveillance technologies are insufficient to adequately patrol the vast volume of cislunar space, and, while space-based sensors are required, the parameter space for sensor placement is non-trivial. In this work, the challenge of maintaining custody of a satellite in cislunar space in the presence of maneuvers of unknown Δv magnitude and time is investigated. Vital regions are first identified and surveillance for a given number of space-based sensors in an optimized surveillance scheme is then established. The CR3BP is employed to model system dynamics and the geometry of the BCR4BP is leveraged to efficiently parameterize visibility conditions and constraints through angular relationships. Δv maneuvers of 0.05 km/s and 0.5 km/s from multiple locations around the planar bifurcating L_2 Lyapunov/halo orbit and the 9:2 synodic resonant NRHO are used to perform a Monte Carlo assessment of key regions for surveillance over a 30-day duration. Cross-sectional maps of each scenario are provided to characterize departure tube structure and assess the significance of maneuver location. Objects departing from the planar orbit are found to exit the orbital vicinity faster and are more likely to escape the Earth-Moon sphere of influence than those emanating from the more energetic NRHO, while NRHO objects are significantly more likely to become trapped in lunar orbits or impact the Moon. The maps reveal clear structures to trajectory departure tubes, that are unique to the maneuver magnitude and orbit type, as well as patterns relative to departure location along the respective orbits. The NRHO objects are additionally found to be, on average, more energetic than their planar L_2 counterparts, and transit a larger volume of cislunar space. Given the massive state space, enhanced surveillance capability is crucial. Using the identified key regions, a volume for surveillance is established. This paper utilizes cost-effective electro-optical sensors, previously proposed for space-based surveillance in the Cislunar region. A visibility count percentage (VCP) is introduced to highlight regions of varying visibility based on user-defined constraints and object parameters. BCR4BP parameterization with the application of Particle Swarm Optimization (PSO) is utilized to offer optimal observers for perturbed NRHO and L2 Lyapunov/halo orbit. Due to the various visibility constraints, the visibility of each object from each observer varies in the region, and hence, the usage of PSO offers the advantage of maximizing the coverage. In the analysis, an observation constellation having observers between two to ten is examined for key regions surveillance. With just one observer, while custody cannot be fully guaranteed, optimal placement can still be identified to maximize the observer's impact. When deploying ten observers optimally, custody is nearly guaranteed, even when accounting for a limiting magnitude of 18 and realistic exclusion angles that restrict visibility. With the increase in the number of optimal observers, the overall number of visible objects increases significantly, giving insights into designing surveillance constellations for full coverage.

REFERENCES

[1] Brian Baker-McEvilly, Surabhi Bhadauria, David Canales, and Carolin Frueh. A comprehensive review on cislunar expansion and space domain awareness. *Progress in Aerospace Sciences*, 147:101019, 2024.

[2] S. Bhadauria, C. Frueh, and K. Howell. Cislunar space domain awareness using bi-circular four body geometry. In *AAS/AIAA Astrodynamics Specialist Conference*, 2022.

[3] Surabhi Bhadauria and Carolin Frueh. Optical observation regions in cislunar space using the bi-circular restricted four body problem geometry. In *2022 Advanced Maui Optical and Space Surveillance Technologies Conference (AMOS)*, 2022.

[4] Surabhi Bhadauria and Carolin Frueh. Optimal optical cislunar space surveillance positioning leveraging the bcr4bp and average visibility. *Journal of Astronautical Sciences (Submitted, Under Review)*, 2024.

[5] Arly Black and Carolin Frueh. Fragmentation characterization in the circular restricted three body problem for cislunar space domain awareness. *Advances in Space Research*, 2024. Submitted, under review.

[6] R. Broucke. Stability of periodic orbits in the elliptic, restricted three-body problem. *AIAA journal*, 7(6):1003–1009, 1969.

[7] Markus Deserno. How to generate equidistributed points on the surface of a sphere. *Max-Planck-Institut fur Polymerforschung*, 99(2):1, 2004.

[8] Robert W Farquhar. A halo-orbit lunar station. *Astronautics and Aeronautics*, 10, 1972.

[9] Robert Willard Farquhar. *The utilization of halo orbits in advanced lunar operations*, volume 6365. National Aeronautics and Space Administration, 1971.

[10] C. Frueh. Lecture notes of course AAE590: Space Traffic Management, Purdue University, Fall 2023.

[11] C. Frueh, K. Howell, K. DeMars, and S. Bhadauria. Cislunar space situational awareness. In *31st AIAA/AAS Space Flight Mechanics Meeting*, 2021.

[12] C. Frueh, K. Howell, K. DeMars, S. Bhadauria, and M. Gupta. Cislunar space traffic management: Surveillance through earth-moon resonance orbits. In *8th European Conference on Space Debris*, 2021.

[13] C. Frueh, B. Little, and J. McGraw. Optical sensor model and its effects on the design of sensor networks and tracking. In *Advanced Maui Optical and Space Surveillance Technologies Conference (AMOS)*, sep 2019.

[14] Carolin Frueh, Kyle Demars, Surabhi Bhadauria, and Kathleen Howell. Cislunar space traffic management: Surveillance through earth-moon resonance orbits. In *8th Eurpoean Conference on Space Debris*, volume 8, 2021.

[15] Michel Hénon. Generating families in the restricted three-body problem; number 52 in lecture note in physics. monographs, 1997.

[16] Kathleen Howell. *AAE 632 Advanced Orbital Dynamics*. School of Aeronautics and Astronautics, Purdue University, 2018.

[17] James Kennedy and Russell Eberhart. Particle swarm optimization. In *Proceedings of ICNN'95-international conference on neural networks*, volume 4, pages 1942–1948. ieee, 1995.

[18] Anne Lemaître. High-order resonances in the restricted three-body problem. *Celestial mechanics*, 32(2):109–126, 1984.

[19] Henri Poincaré. *Les méthodes nouvelles de la mécanique céleste*, volume 3. Gauthier-Villars et fils, imprimeurs-libraires, 1899.

[20] Rohith Reddy Sanaga. Personal communication. Purdue University.

[21] F. Sanson and C. Frueh. Noise quantification in optical observations of resident space objects for probability of detection and likelihood. In *AAS/AIAA Astrodynamic Specialist Conference, Vail, CO*, 2015. 15-634.

[22] F. Sanson and C. Frueh. Noise estimation and probability of detection in nonresolved images: Application to space object observation. *Advances in Space Research*, 64:1432 – 1444, 2019.

[23] Wolfgang Seefelder. *Lunar Transfer Orbits Utilizing Solar Perturbations and Ballistic Capture*. Herbert Utz Verlag, 2002.

[24] Yuhui Shi and Russell Eberhart. A modified particle swarm optimizer. In *1998 IEEE international conference on evolutionary computation proceedings. IEEE world congress on computational intelligence (Cat. No. 98TH8360)*, pages 69–73. IEEE, 1998.

[25] Emily M Zimovan Spreen. *Trajectory design and targeting for applications to the exploration program in cislunar space*. PhD thesis, Purdue University, 2021.

[26] Travis Swenson, Martin Lo, Brian D Anderson, and Thomas Gorordo. The topology of transport through planar lyapunov orbits. In *2018 Space Flight Mechanics Meeting*, page 1692, 2018.

[27] Victor Szebehely and FT Geyling. Theory of orbits: The restricted problem of three bodies. 1968.

[28] Emily M Zimovan, Kathleen C Howell, and Diane C Davis. Near rectilinear halo orbits and their application in cis-lunar space. In *3rd IAA Conference on Dynamics and Control of Space Systems, Moscow, Russia*, volume 20, page 40, 2017.